Journal of Biomedical Optics 9(3), 587–592 (May/June 2004)

Near-infrared autofluorescence imaging for detection of cancer

Stavros G. Demos
Lawrence Livermore National Laboratory
PO Box 808, L-411
Livermore, California 94551
and
UC Davis Cancer Center
4501 X Street
Sacramento, California 95817

Regina Gandour-Edwards
Rajen Ramsamooj
Ralph deVere White
UC Davis Cancer Center
4501 X Street
Sacramento, California 95817

Abstract. Near-infrared autofluorescence imaging of tissues under long-wavelength laser excitation in the green and red spectral region complemented by cross-polarized elastic light scattering was explored for cancer detection. Various types of normal and malignant human tissue samples were utilized in this investigation. A set of images for each tissue sample was recorded that consisted of two autofluorescence images obtained under 532- and 632.8-nm excitation and light-scattering images obtained under linearly polarized illumination at 700, 850, and 1000 nm. These images were compared with the histopathology of the tissue sample. The experimental results indicated that for various tissue types, the intensity of the autofluorescence integrated over the 700 to 1000-nm spectral region was considerably different in cancer tissues than in that of the contiguous non-neoplastic tissues. This difference provided the basis for the detection of cancer and delineation of the tumor margins. Variations on the relative intensity were observed among different tissue types and excitation wavelengths. [DOI: 10.1117/1.1688812]

Keywords: near-infrared; cancer; autofluorescence.

Paper 02076 received Nov. 5, 2002; revised manuscript received May 16, 2003 and Jun. 19, 2003; accepted for publication Aug. 22, 2003.

1 Introduction

Optical spectroscopy has been widely used to acquire fundamental knowledge about physical, chemical, and biological processes that occur in biomaterials. Various research groups have attempted to classify and diagnose tissue states using fluorescence and Raman spectroscopy.[1] Although most of the published work is associated with the detection and imaging of malignancies in human tissues, including the cervix, bladder, lung, breast, esophagus, stomach, uterus, skin, and colon,[2–9] tissue autofluorescence has shown promise in assisting in other clinical applications such as the diagnosis of atherosclerosis[10] and Alzheimer's disease.[11] The main fluorophores in tissues exhibit maximum absorption at photon energies higher than 2 eV. As a result, most tissue spectroscopy research has employed UV to visible light sources from 250 to 550 nm. The disadvantage of these excitation wavelengths is their short penetration depth in tissues, which leads to extraction of information only from superficial tissue layers.

Raman-scattering measurements in tissues are performed in the near-infrared (NIR) spectral region to avoid emission by tissue chromophores. However, even at these longer wavelengths, the presence of a long Stokes spectral wing is observed,[12–13] which makes the observation of the fine details in the Raman-scattering spectrum difficult. The intensity of the Stokes spectral wing becomes weaker as the pump wavelength increases.[12] This spectral wing has been considered to be noise and is usually subtracted from the Raman spectral profile using complex fitting parameters to acquire the spectral features associated with the Raman active vibrational and/or rotational modes. It was only recently shown that the origin of this background signal in the far red and near-infrared spectral region in Raman-scattering measurements of tissues is due to emission by photoexcited fluorophores.[14] The lifetime of this emission was found to be on the order of 1 ns, which is similar to that of other tissue fluorophores. It was also demonstrated in the same paper that the NIR autofluorescence intensity from cancer and normal human breast tissue is distinctly different, suggesting a new way to detect breast cancer.

The objective of this work was to investigate the ability of native tissue fluorescence under long-wavelength laser excitation in combination with NIR polarized light scattering to image tissue components, with special attention to detecting cancer and distinguishing it from noncancerous tissues. Our experimental approach involved imaging in the 700 to 1000-nm spectral region of various types of malignant tissues with contiguous non-neoplastic human tissue samples using cross-polarized elastic light scattering and tissue autofluorescence under 532- and 632.8-nm laser excitation. The optical images were then compared with the histological map of the specimen to determine which imaging technique can detect cancer and outline tumor margins.

2 Experimental Arrangement

The human tissue specimens studied in this work were obtained fresh from surgical resections. The experiments preceded tissue fixation to ensure no compromise of tissue char-

Address all correspondence to Stavros G. Demos, Lawrence Livermore National Laboratory, PO Box 808, L-411, Livermore, California 94551. Tel: 925-423-3388; FAX: 925-423-2463; E-mail: demos1@llnl.gov

1083-3668/2004/$15.00 © 2004 SPIE

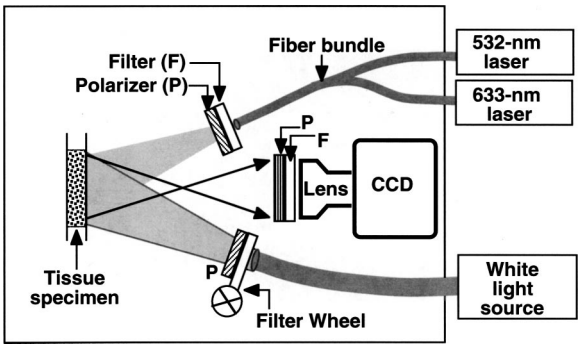

Fig. 1 Schematic layout of the key optical components of the instrumentation for performing *in vitro* measurements of human tissue samples immediately after surgery. The experimental setup involves polarizers (P) and appropriate optical filters (F). Two lasers and a white light source coupled with optical fibers are used to illuminate the sample.

acteristics. To simplify the procedure for optical spectroscopy experiments on human samples, we built a compact spectroscopic imaging system that was positioned in a laboratory space adjacent to the surgical pathology unit at the University of California-Davis Medical Center in Sacramento, California. This allowed us to perform *in vitro* measurements of human tissue specimens as they became available immediately after surgery without interfering with standard hospital procedures.

Figure 1 shows the schematic layout of the key optical components composing this spectroscopic imaging unit. The human tissue specimens were positioned between two parallel glass slides located on a sample holder and were slightly compressed to an approximately uniform thickness that was in the range of 1 to 5 mm, depending on the original thickness of the specimen. The images of the specimens were acquired using a liquid nitrogen-cooled CCD detector coupled to a camera lens. A polarizer was positioned in front of the camera lens and its polarization orientation was controlled by the operator. In addition, a 700-nm long-pass (LP) filter was positioned in front of the camera lens. For the autofluorescence imaging experiments, the photoexcitation was provided by a 632.8-nm helium:neon (He:Ne) laser and by a 532-nm diode-pumped laser. The laser light was transmitted to the imaging compartment of the system using optical fibers. The diverging output beams from each fiber were used to provide nearly uniform illumination of the sample. A narrow-band interference filter was positioned in front of the output of the fiber to ensure monochromatic illumination. The 700 LP filter located in front of the CCD, in combination with the response spectrum of the CCD imaging camera, determined the spectral range of the light emitted by the tissue (700 to 1000 nm) that was selected for image acquisition. This spectral range used to record the autofluorescence images of the tissues was the same for both 532- and 632.8-nm excitation.

For the light-scattering imaging experiments, a white light source coupled to a fiber bundle was used to illuminate the sample. Three illumination wavelengths were used at 700, 850, and 1000 nm, which were selected by 40-nm bandwidth interference filters positioned on a filter wheel located at the output of the fiber bundle. A polarizer was positioned at the output of this fiber bundle. With this imaging system, a set of eight images was recorded for each sample. More specifically, we recorded the parallel and the cross-polarized light-scattering images under 700, 850, and 1000-nm illumination and the NIR (700- to 1000-nm) autofluorescence images under 532- and 632.8-nm excitation. Interimage operations permitted the acquisition of additional information. The ratio between cross-polarized light-scattering images recorded under different illumination wavelengths (700, 850, or 1000 nm) using pixel-by-pixel interimage division between the digitally recorded images, can image the change in the scattering properties of the tissue components as a function of the wavelength. Similarly, a division between autofluorescence images obtained under different excitation wavelengths or between autofluorescence and light-scattering images helped enhance the visibility of the features of interest. In addition, using the two orthogonal polarization light-scattering image components for each illumination wavelength, we obtained the degree of polarization of the light-scattering images for each wavelength. These images were subsequently compared with the histopathology map of this same tissue specimen. A pathologist viewed the corresponding hematoxylin and eosin (H&E)-stained paraffin section by light microscopy and prepared an outline of the cancer and the noncancerous areas. Specimens obtained from more than 80 patients have been studied to date.

3 Experimental Results

In this paper we discuss illustrative examples of our experimental observations. The aim is to demonstrate the potential of this approach for imaging tissue components. Figure 2 shows images of a 4-cm×3-cm human breast tissue, 5 mm thick, with a multifocal high-grade ductal carcinoma surrounded by fibrous supporting tissue and with an adjacent area of fatty infiltration. Figures 2(a) and 2(b) show the near-infrared autofluorescence (NIRA) images under 532- and 632.8-nm laser excitation, respectively. Figure 2(c) shows a cross-polarized light-scattering (CPLS) image under 700-nm illumination. Figure 2(d) shows a ratio of the NIRA image shown in Fig. 2(b) divided by the CPLS image shown in Fig. 2(c). Figure 2(e) shows an interimage ratio of the CPLS image under 1000-nm illumination divided by the CPLS image at 700 nm. Figure 2(f) shows an interimage ratio of the CPLS image at 700 nm divided by the NIRA image under 532-nm illumination.

From the images of the specimen shown in Fig. 2, only the NIR fluorescence image under 632.8-nm excitation [Fig. 2(b)] and the resulting ratio image shown in Fig. 2(d) demonstrate a correlation with a cancer identified by histology. The ≈1-mm diameter ductal carcinoma areas appear as features with higher emission intensity under 632.8-nm excitation [see Fig. 2(b)]. The ratio image shown in Fig. 2(d) improves the visibility and contrast of the cancer and provides sharper delineation of the tumor margins.

Figure 2(g) shows the digitized intensity along a transverse and a vertical direction of the NIRA image under 632.8-nm excitation. The transverse (vertical) profile represents the integrated intensity over 3 vertical (transverse) pixels of the digital image (1 mm=6.1 pixels). The inset shows the NIRA image [the same as that shown in Fig. 2(b)] where the direc-

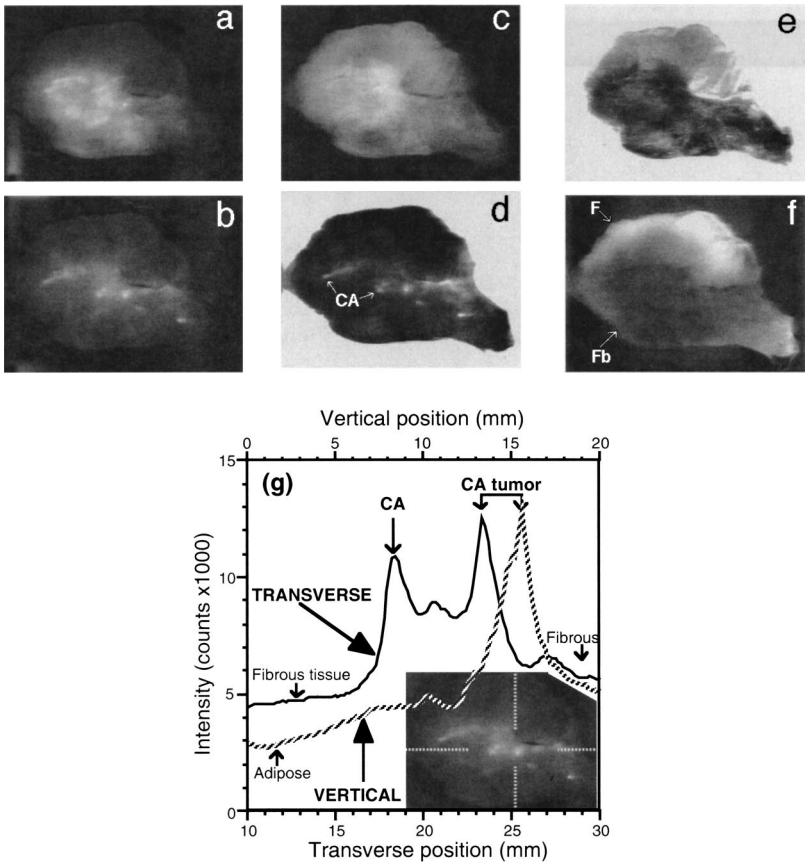

Fig. 2 Images of a human breast tissue sample with a multifocal high-grade ductal carcinoma. NIR autofluorescence images in the 700- to 1000-nm spectral region under (a) 532-nm and (b) 633-nm laser excitation. (c) Cross-polarized light scattering under 700-nm illumination. (d) to (f) Ratio images to enhance visibility of tissue components. (g) The digitized intensity along a transverse and a vertical direction of the NIRA image under 632.8-nm excitation. More details are provided in the text. CA, cancer; F, adipose tissue; Fb, fibrous tissue.

tions used to obtain the intensity profiles are indicated with dotted lines. The two 3-pixel stripes are intersecting at the largest cancer nodule observed in this image. The horizontal axis of the intensity profiles indicates the distance (in millimeters) from the left side edge of the specimen along the transverse direction, and from the upper edge of the specimen along the vertical direction. These profiles demonstrate that there is a considerable difference in the NIR emission intensity arising from these cancerous areas compared with that from the surrounding normal tissue—by a factor of about 2.5 compared with fibrous tissue and a factor of 4 compared with adipose tissue. Figures 2(e) and 2(f) show with higher intensity the presence of adipose tissue in the upper part of the specimen.

By defining the relative intensity difference ΔI_{ca} as

$$\Delta I_{ca} = (I_{cancer} - I_{normal})/I_{normal}$$

where I_{normal} is the average image intensity of the fibrous normal tissue and I_{cancer} is the average image intensity of cancer tissue, we find that in the case of the specimen shown in Fig. 2, $\Delta I_{ca} \approx 1.5$ for the image shown in Fig. 2(b) and $\Delta I_{ca} \approx 1.6$ for the image in Fig. 2(d). The average intensity was estimated from four different 36-pixel (1-mm^2) areas in the image of the fibrous part of the tissue and, owing to their small size, over four different 9-pixel areas in the center of cancer nodules. In the examples that follow, the average image intensity was measured as described for the case of fibrous tissue.

Figure 3 shows a set of images obtained from a liver specimen. A histological section of this specimen shows a well-

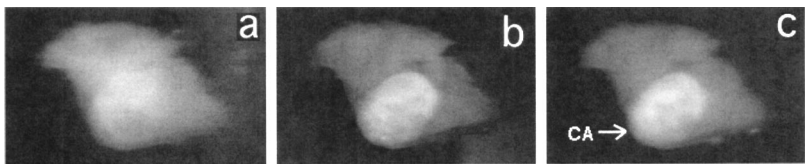

Fig. 3 Images of a human liver tissue sample with hepatoblastoma. (a) Cross-polarized light-scattering image at 700 nm. NIR fluorescence images under (b) 532-nm and (c) 632.8-nm excitation. CA, cancer.

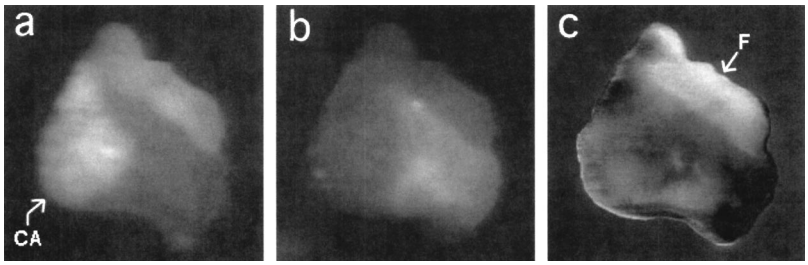

Fig. 4 Images of a human kidney tissue with renal cell carcinoma. (a) Cross-polarized image at 700 nm. (b) NIR fluorescence images under 632.8-nm laser excitation. (c) Ratio of NIR autofluorescence image under 532-nm excitation over that under 632-nm excitation. CA, cancer; F, fat.

circumscribed 0.8×0.5-cm nodule of a hepatoblastoma. Figure 3(a) shows the CPLS image under 700-nm illumination. Figures 3(b) and 3(c) show the NIRA images under 532- and 632.8-nm laser excitation, respectively. The cancer nodule is visible in all images shown in Fig. 3 as a feature that is brighter in intensity. The digitized intensity in the area of the cancer nodule in the CPLS image shown in Fig. 3(a) is higher than that of the adjacent normal liver tissue with $\Delta I_{ca} \approx 0.13$. This intensity difference between the two tissue components is further increased in the NIRA images and it becomes $\Delta I_{ca} \approx 0.4$ and $\Delta I_{ca} \approx 0.65$ under 532- and 632.8-nm excitation, respectively. This difference in image intensity allows the best visualization of the cancer nodule, especially in the NIRA images [Figs. 3(b) and 3(c)].

Figure 4 shows images of a kidney containing a cancerous lesion. Figure 4(a) shows the CPLS image under 700-nm illumination. Figure 4(b) shows the NIRA image under 632.8-nm laser excitation. Figure 4(c) is the image obtained from a division of the NIRA image under 532-nm excitation over that recorded under 632.8-nm excitation. The pathological examination shows a poorly demarcated nodule of a renal cell carcinoma measuring 1.0×0.6 cm. This tumor is surrounded by normal kidney. The upper side of the specimen is normal fat tissue that surrounds the kidney. In the optical images, the cancer appears brighter in intensity in the CPLS images [Fig. 4(a)] and darker in the NIRA images [Fig. 4(b)] compared with the normal kidney. In the CPLS image under 700-nm illumination, $\Delta I_{ca} \approx (+)0.7$, while for the NIRA image under 632.8-nm excitation, $\Delta I_{ca} \approx (-)0.4$. The fat located on the upper side of this specimen (as imaged) is better visualized in the ratio image shown in Fig. 4(c), where it is clearly differentiated from the kidney tissue. In the latter image, normal kidney tissue cannot be differentiated from the cancer.

Figure 5 shows NIRA images under 632.8-nm excitation from human tissue samples containing cancers in a field of normal tissue from pancreas, prostate, and bladder in three different patients. Figure 5(a) shows the NIRA image from a ≈3.3-cm×2.3-cm×4-mm cross-section of pancreas containing an area of cancer in the middle. The tumor appears as a brighter feature than the normal surrounding tissue, with $\Delta I_{ca} \approx 0.7$. The cancer is also visible in the NIRA image under 532-nm excitation and in the CPLS images having $\Delta I_{ca} \approx 0.7$ and $\Delta I_{ca} \approx 0.25$, respectively.

Figure 5(b) shows the NIRA image under 632.8-nm excitation of a ≈4-cm×3-cm×5-mm cross-section of human prostate. The 5-mm×3-mm area of prostatic adenocarcinoma within the peripheral zone is clearly visible in the image as a brighter feature compared with that of the normal tissue, having $\Delta I_{ca} \approx 2.5$. This feature is barely visible in the CPLS images, having slightly lower intensity than the adjacent normal tissue, but the contrast is not sufficient for a definite conclusion or for determination of the tumor's margins. The cancer is also visible in the NIRA image under 532-nm

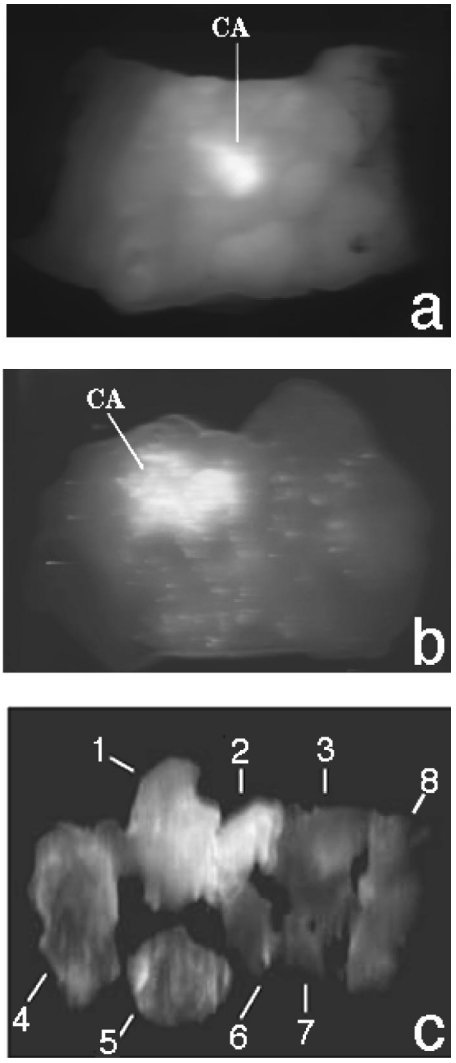

Fig. 5 NIR autofluorescence images under 632.8-nm laser excitation from (a) pancreas, (b) prostate, and (c) bladder tissues containing normal and cancer (CA) components.

excitation, with $\Delta I_{ca} \approx 0.5$. The submillimeter-diameter features observed in the NIR autofluorescence image that are brighter in intensity than normal tissue are caused by corpora amylacea (protein concretions). These features can be discriminated from cancers by recording the degree of polarization image of the NIR autofluorescence from this tissue because they preserve polarization to a much higher degree than the rest of the tissue components. This imaging method is not discussed in this paper.

Figure 5(c) shows the NIRA image from eight small (5 mm in diameter or less) bladder samples from the same patient obtained by transurethral resection. The samples were compressed between glass slides to a uniform thickness of approximately 1 mm. In this image, the two specimens that exhibit higher intensity (labeled 1 and 2) are normal. Two specimens (4 and 5) contain both normal and cancer areas. The remaining specimens are diffusely permeated with cancer. These results are typical of our observations of bladder tissues, which show that bladder cancer exhibits lower emissivity than normal bladder tissue in the NIR spectral region. In the NIRA images obtained under 532 and 632.8 nm, the emission intensity of the cancer (3, 6 to 8) is lower than the average emission of the normal tissue, with $\Delta I_{ca} \approx -0.7$ and $\Delta I_{ca} \approx -0.3$, respectively. In addition, cancer was also visible in the CPLS images, with $\Delta I_{ca} \approx -0.2$.

4 Discussion

Our experimental results suggest that when differences exist in the scattering properties of tissue components, cross-polarized light-scattering images provide better image quality than unpolarized or parallel-polarized images. This finding is not surprising since the cross-polarization removes the specular reflections on the sample's surface from the image. In addition, the cross-polarized image is formed by photons that have propagated inside the tissue before backscattering, and as a result they have interacted with the tissue over larger optical distances than photons that maintained their polarization state.[15] From the polarization-sensitive light-scattering images, one can also obtain the degree of polarization image, which depicts the way light depolarizes during interaction with different tissue components. This property has been discussed elsewhere.[16]

The NIRA image shown in Fig. 2(b) demonstrates that this method can detect small lesions (1 mm or smaller) in a field of normal tissue. The experimental results shown in Fig. 3 and Fig. 4 indicate that the measured intensity of the NIRA signal of the different tissue components is not largely dependent on their corresponding light-scattering properties. The CPLS signals from the tumor in liver and kidney (shown in Fig. 3 and Fig. 4) are higher than that of the corresponding normal tissue. However, the intensity of the NIRA from the tumor in kidney is lower than that of the normal tissue, while the opposite is the case in liver. The sensitivity for cancer detection using NIR autofluorescence can be enhanced by utilizing excitation at the appropriate wavelengths. The 1-mm tumor lesions in the breast specimen shown in Fig. 2 are visible in the NIR autofluorescence images under 632.8-nm excitation, but not under 532-nm excitation.

It is known that among the principal tissue chromophores, only porphyrins exhibit absorption in the red spectral region, accompanied by emission in the far-red and near-infrared region.[17] Porphyrin compounds are also utilized in photodynamic therapy using localized laser excitation, usually in the 620- to 640-nm wavelength region. Porphyrin biosynthesis in tumoral cells was first investigated nearly 40 years ago as a result of a suspected association of cancer with the porphyrias (a disease in which the predominant symptoms were due to skin photosensitivity). It has been observed that the content of porphyrins in the liver and the tumor of patients with cancer was elevated.[18–23] Our experimental result showing enhancement of the NIR fluorescence in liver cancer tumors is in agreement with these reports, supporting the hypothesis that the observed emission is predominantly due to porphyrins.

It has also been reported that significantly higher levels of porphyrins and precursors were found in other types of cancer compared with the normal tissue of origin.[24–28] Interesting results were described in Ref. 26, where it is suggested that the level of porphyrins in primary internal organ tumors was greater and in endocrine gland tumors less than in their contiguous non-neoplastic tissues.

Assuming that the NIR autofluorescence signal under long-wavelength excitation arises mainly from porphyrins, the imaging method discussed in this work may offer a way to monitor and/or image the porphyrin content in tissues. The strong evidence that the heme-biosynthetic pathway, and therefore the production of porphyrins, is disturbed in neoplasia may be the reason that the NIR autofluorescence images offer, in many cases, high contrast between normal and tumor tissue. Our results show that although in some cases the emissivity of cancer tissue is higher than the normal host tissue, such as in liver and breast, this is not always the case. Typical examples of the latter case are the kidney and bladder, where the NIRA emission from cancer is lower than that of the normal tissue. One should not ignore the possibility that part of the NIR emission may arise from biomolecules other than porphyrins, which may also be unevenly distributed between normal and cancer tissues. Independent of the origin of the differences in the NIR emission intensity, an imaging system that is based on this method could assist a surgeon in visualizing the tumor margins for more accurate and complete removal of cancerous tissue. In addition, identification of the relation of the biomolecules that give rise to the NIR fluorescence with the biochemistry and metabolism of the tumor may provide a useful method for *in vivo* assessment of the status of the tumor and its behavior under different treatment protocols.

The experimental results discussed here suggest that NIR autofluorescence under long-wavelength excitation, in combination with cross-polarized light scattering, is a promising approach for detecting and imaging in real time cancers residing in multiple sites of the human body.

The fact that we are using for photoexcitation and imaging longer wavelengths that penetrate the tissue more efficiently can be considered an advantage because we can probe a larger tissue volume and not only the surface, and can minimize concerns regarding tissue damage. As is apparent from the representative experimental results discussed in this paper, we have not identified a unique or typical pattern that describes all types of cancers. However, the experimental results indicate a characteristic and consistent behavior for each cancer type. The results shown in Fig. 2 from breast cancer are in agreement with results previously reported regarding the NIR

autofluorescence of breast cancer.[14] The results from liver cancer shown in Fig. 3, which demonstrate enhanced NIR emission from the tumor, are in agreement with previous observations of elevated porphyrin content in liver tumors.[18,23] A detailed report on our results from bladder cancer has been submitted for publication and shows a consistent behavior in specimens from 25 patients. It must be pointed out that the results shown here are from tissues that did not involve necrosis. The presence of necrotic tissue leads to a large increase in the NIR autofluorescence, which is in agreement with a previous report using violet light excitation.[29]

Acknowledgments

This work was performed in part at Lawrence Livermore National Laboratory under the auspices of the U.S. Department of Energy under contract W-7405-Eng-48 through the Institute for Laser Science and Applications. This research is supported by the California Cancer Research Program and the California Breast Cancer Program.

References

1. G. A. Wagnieres, W. M. Star, and B. C. Wilson, ''In vivo fluorescence spectroscopy and imaging for oncological applications,'' *Photochem. Photobiol.* **68**(5), 603–632 (1998) and references therein.
2. R. R. Alfano, B. Tata, J. Cordero, P. Tomashefsky, F. W. Longo, and M. A. Alfano, ''Laser-induced fluorescence spectroscopy from native cancerous and normal tissues,'' *IEEE J. Quantum Electron.* **QE-20**, 1507–1511 (1984).
3. J. R. Mourant, I. J. Bigio, J. Boyer, R. L. Conn, T. Johnson, and T. Shimada, ''Spectroscopic diagnosis of bladder cancer with elastic light scattering,'' *Lasers Surg. Med.* **17**, 350–357 (1995).
4. K. T. Schomacker, J. K. Frisoli, C. C. Compton, T. J. Flotte, J. M. Richter, N. S. Nishioka, and T. F. Deutsch, ''Ultraviolet laser-induced fluorescence of colonic tissue—basic biology and diagnostic potential,'' *Lasers Surg. Med.* **12**, 63–78 (1992).
5. A. Pradhan, B. B. Das, K. M. Yoo, J. Cleary, R. Prudente, E. Celmer, and R. R. Alfano, ''Time-resolved UV photoexcited fluorescence kinetics from malignant and non-malignant human breast tissues,'' *Lasers Life Sci.* **4**, 225–234 (1992).
6. Y. Yang, A. Katz, E. J. Celmer, M. Z. Szczepanik, and R. R. Alfano, ''Optical spectroscopy of benign and malignant breast tissues,'' *Lasers Life Sci.* **7**(2), 115–127 (1996).
7. T. D. Wang, J. VanDam, J. M. Crawford, E. A. Preisinger, Y. Wang, and M. S. Feld, ''Fluorescence endoscopic imaging of human colonic adenomas,'' *Gastroenterology* **111**, 1182–1191 (1996).
8. N. Ramanujam, M. F. Mitchell, A. MahadevanJansen, S. L. Thomsen, G. Staerkel, A. Malpica, T. Wright, N. Atkinson, and R. Richards-Kortum, ''Cervical precancer detection using a multivariate statistical algorithm based on laser-induced fluorescence spectra at multiple excitation wavelengths,'' *Photochem. Photobiol.* **64**, 720–735 (1996).
9. B. Kulapaditharom and V. Boonkitticharoen, ''Laser-induced fluorescence imaging in localization of head and neck cancers,'' *Ann. Otol. Rhinol. Laryngol.* **107**, 241–246 (1998).
10. C. Kittrell, R. L. Willett, C. S. Pacheo, N. B. Ratliff, J. R. Kramer, E. G. Malk, and M. S. Feld, ''Diagnosis of fibrous arterial atherosclerosis using fluorescence,'' *Appl. Opt.* **24**(15), 2280–2281 (1985).
11. E. B. Hanlon, I. Itzkan, R. R. Dasari, M. S. Feld, R. J. Ferrante, A. C. McKee, D. Lathi, and N. W. Kowall, ''Near-infrared fluorescence spectroscopy detects Alzheimer's disease in vitro,'' *Photochem. Photobiol.* **70**, 236–242 (1999).
12. C. J. Frank, D. C. Redd, T. S. Gansler, and R. L. McCreery, ''Characterization of human breast specimens with near-IR Raman spectroscopy,'' *Anal. Chem.* **66**(3), 319–326 (1994).
13. J. J. Baraga, M. S. Feld, and R. P. Rava, ''Rapid near-infrared Raman spectroscopy of human tissue with a spectrograph and CCD detector,'' *Appl. Spectrosc.* **46**(2), 187–190 (1992).
14. G. Zhang, S. G. Demos, and R. R. Alfano, ''Far-red and NIR spectral wing emission from tissues under 532-nm and 632-nm photoexcitation,'' *Lasers Life Sci.* **9**, 1–16 (1999).
15. S. G. Demos and R. R. Alfano, ''Optical polarization imaging,'' *Appl. Opt.* **36**, 150–155 (1997).
16. S. G. Demos, A. J. Papadopoulos, H. Savage, A. S. Heerdt, S. Schantz, and R. R. Alfano, ''Polarization filter for biological optical imaging,'' *Photochem. Photobiol.* **66**, 821–825 (1997).
17. K. Kalyanasundaram, *Photochemistry of Porphyridine and Porphyrin Complexes*, Chapter 13 and references therein, Academic Press, London (1991).
18. K. Keczkes and D. J. Barker, ''Malignant hepatoma associated with acquired hepatic cutaneous porphyria,'' *Arch. Dermatol.* **11**, 72–82 (1976).
19. T. H. Tio, B. Leijnse, A. Jarret, and C. Rimington, ''Acquired porphyria from a liver tumor,'' *Clin. Sci.* **16**, 517–525 (1957).
20. R. P. H. Thompson, D. C. Nicholson, T. Farnan, D. N. Whitmore, and B. Williams, ''Cutaneous porphyria due to a malignant primary hepatoma,'' *Gastroenterology* **59**, 779–783 (1970).
21. L. Rasetti, G. F. Rubino, L. Tettinatti, and G. W. Drago, ''Porphyrin porphobilinogen and amino ketone levels in tumor tissue,'' *Panminerva Med.* **7**, 105–110 (1965).
22. R. Belcher, S. G. Smith, D. C. Nicholson, and R. Williams, ''Study of porphyrins present in hepatoma tissue,'' *Biochem. J.* **119**, 16–22 (1970).
23. R. T. Waddington, ''A case of primary liver tumor associated with porphyria,'' *Br. J. Surg.* **59**, 653–654 (1972).
24. C. A. Pierach, I. C. Bossenmaier, R. A. Cardinal, and M. Weimer, ''Pseudo-porphyria in a patient with hepatocellular carcinoma,'' *Am. J. Med.* **76**, 545–548 (1984).
25. S. Rayhanzadeh, R. G. Shoss, J. Noyes, and N. Y. Albany, ''Porphyria cutanea tarda associated with lymphosarcoma,'' *Arch. Dermatol.* **111**, 129–132 (1975).
26. B. Zawirska, ''Comparative porphyrin content in tumors with contiguous non-neoplastic tissues,'' *Neoplasma* **26**, 223–229 (1979).
27. N. Schoenfeld, O. Epstein, M. Lahav, R. Mamet, M. Shaklai, and A. Atsmon, ''The heme biosynthetic pathway in lymphocytes of patients with malignant lymphoproliferative disorders,'' *Cancer Lett.* **43**, 43–48 (1988).
28. M. M. H. El-Sharabasy, A. M. El-Wassel, M. M. Hafez, and S. A. Salim, ''Porphyrin metabolism in some malignant diseases,'' *Br. J. Cancer* **65**, 409–412 (1992).
29. D. M. Harris and J. Werkhaven, ''Endogenous porphyrin fluorescence in tumors,'' *Lasers Surg. Med.* **7**, 467–472 (1987).